High-pressure drop rates in solid-state batch one-step scCO2 foaming of acrylic polymers: A way to stabilize the structure of micro-nano foams

Margaux Haurat, Yannick Anguy, Cécile Gaborieau, Guillaume Aubert, Cyril Aymonier, Michel Dumon

To cite this version:

Margaux Haurat, Yannick Anguy, Cécile Gaborieau, Guillaume Aubert, Cyril Aymonier, et al.. High-pressure drop rates in solid-state batch one-step scCO2 foaming of acrylic polymers: A way to stabilize the structure of micro-nano foams. Chemical Engineering Science, 2023, 281, pp.119099. ⟨10.1016/j.ces.2023.119099⟩. ⟨hal-04186228⟩

HAL Id: hal-04186228

https://hal.science/hal-04186228v1

Submitted on 24 Aug 2023

HAL is a multi-disciplinary open access archive for the deposit and dissemination of scientific research documents, whether they are published or not. The documents may come from teaching and research institutions in France or abroad, or from public or private research centers.

L'archive ouverte pluridisciplinaire **HAL**, est destinée au dépôt et à la diffusion de documents scientifiques de niveau recherche, publiés ou non, émanant des établissements d'enseignement et de recherche français ou étrangers, des laboratoires publics ou privés.

Autorisation HAL

HAL Authorization

High-pressure drop rates in solid-state batch one-step $scCO_2$ foaming of acrylic polymers: a way to stabilize the structure of micro-nano foams

Margaux Haurat[1], Yannick Anguy[2*], Cécile Gaborieau[2], Guillaume Aubert[3], Cyril Aymonier[3], Michel Dumon*[1]

[1] Université de Bordeaux, UMR CNRS 5629, Bordeaux INP, LCPO, UMR 5629, ENSCBP 16 avenue Pey Berland, F-33600 Pessac, France
[2] Université de Bordeaux, UMR CNRS 5295 I2M, F-33405, Talence, France
[3] Université de Bordeaux, UMR CNRS 5026, Bordeaux INP, ICMCB, UMR 5026, F-33600 Pessac, France

*Contact authors to whom correspondence should be addressed: yannick.anguy@u-bordeaux.fr and michel.dumon@u-bordeaux.fr

Abstract

One-step solid-state batch $scCO_2$ foaming is used with the target of achieving acrylic polymer micro-nano foams. Foaming is triggered by an average pressure drop (APDR), covering two decades, from 0.3 to 30 $MPa.s^{-1}$. This study principally addresses the combined beneficial effects of block copolymer addition (BCP, here denoted as MAM) and high APDR. Numerous subtle kinetic parameters actually interplay and compete in the production of the final foams. In particular, the material effective temperature, the effective glass transition temperature of the plasticized system and the instantaneous PDR are physical quantities each having their own kinetics during foaming. The resulting foam morphologies are quantified by SEM microscopy and image analysis. A high APDR and the presence of BCP are shown to play a key role in the final structure of the foams. Over the scrutinized range of saturation temperature (40 °C to 60 °C *i.e.* rather 'low' temperatures in the CO_2 supercritical state), the APDR is the main factor for significantly reducing cell size and increasing nuclei density in foams from neat PMMA. In the block copolymer approach, increasing the APDR is of secondary importance as the targeted reduction of the porosity dimensions and augmentation of nuclei density are mostly the consequence of MAM presence. In this latter case, increasing the APDR still promotes the 'efficiency' of the BCP nucleants. A real efficient nucleation activity of MAM additive is observed at a very high APDR (30 $MPa.s^{-1}$), leading to monomodal homogeneous distribution of tiny pores in nearly nanosized foams. At lower APDR, an interesting reproducible double porosity (foams containing intra-wall and inter-cell pores) is detected in PMMA/MAM systems. In such double porosity foams, benefits from the Knudsen effect achieved within well expanded local domains (showing micron-sized pores) may remain meaningful thanks to a locally poorly expanded nanoporous thick solid skeleton encapsulating these local domains. Thereby, the radiative thermal conduction can be minimized and does not override the conductive component at the sample scale. This work provides further insight on acrylic polymer BCP foams influenced by different kinetics.

Keywords: supercritical carbon dioxide; micro-nano foams; one-step batch foaming; high-pressure drop rate; acrylic polymers; quantitative structural analysis; foaming process; thermal insulation

1. Introduction

In recent years, polymer foams, and especially micro-nano foams obtained by a blowing (or foaming) agent, have raised the interest of industrials and academics due to their expected unusual combination of properties. Indeed, reducing the foam porosity dimensions from micro to nano range can lead to improved mechanical and thermal insulation properties (e.g. due to the Knudsen effect for the latter) [1],[2], or even filtration properties. However, when a blowing agent is used, the desired porosity size reduction is not easy to reach and requires optimization of the foaming process conditions (e.g. saturation pressure, temperature, and time, pressure drop rate) for each foaming agent – material – process combination.

The foaming agent is either chemical or physical. Chemical foaming requires use of a chemical blowing agent to generate a gas by thermal decomposition or by chemical reaction [3]. On the contrary, a physical blowing agent (e.g. an inert gas) is directly injected in the process [4],[5],[6]. In both cases, a thermodynamic instability is required to induce a phase separation between the gas and the material. At that point, foaming is initiated and the nucleation, growth and coalescence steps ensue. Depending on the foaming conditions, all three steps may, or not, partially overlap over time.

In order to propose a more environmental responsible alternative than chemical foaming, carbon dioxide (CO_2) is selected as the physical blowing agent. This non-toxic and low-cost blowing agent enters the supercritical state ($scCO_2$) in rather easy conditions, with a critical point at $P_C = 7.38\ MPa$ and $T_C = 31\ °C$. In these specific conditions, CO_2 offers a combination of liquid and gaseous properties *i.e.* good solubility and diffusivity in polymers (in comparison with other physical blowing agents, e.g. nitrogen) [7]. The supercritical specificities are thus favorable for polymer saturation and to some extent for polymer foaming (as pressure is released, the blowing agent leaves rapidly the supercritical state).

Considering the high CO_2-philicity and the ability to foam with reduced porosity dimensions of acrylic polymers, they are good candidates for $scCO_2$-assisted saturation/foaming [8],[9]. Both neat poly(methyl methacrylate) (PMMA) and blends of PMMA + MAM – the so-called MAM is a triblock copolymer PMMA-PBA-PMMA (where PBA is poly(butyl acrylate)) – have been largely studied in the literature and were selected for this study. In a 90/10 PMMA/MAM weight ratio solid precursor blend, MAM structures are typically nano micellar-like objects dispersed in the PMMA matrix. Due to the higher CO_2-philicity of the soft PBA block, the micellar objects concentrate the CO_2 and act as CO_2-reservoirs during saturation and foaming. In the foaming process, the micellar objects are deemed to act as effective nucleation sites (as other additives [10]) and to improve PMMA foaming (foam homogeneity and cell size reduction) [6],[11],[12],[13].

Acrylic polymers can be saturated and foamed using various processes assisted with $scCO_2$; one can quote extrusion [4],[14], injection [5],[15] and batch foaming (either one-step or two-step) [6],[11],[16]. So far, batch foaming (or autoclave foaming) is preferred over the other processes to produce foams with small porosities [12],[16]. Indeed, contrary to other processes, all batch saturation conditions (*i.e.* saturation pressure, temperature and time), are independently controlled [8]. In view of solid-state one-step batch foaming with reduced porosity dimensions, the roles of the saturation pressure and temperature upon acrylic polymers-foaming are well known [17],[18]. On the one hand, saturation pressure (P^{sat}) has to be maximized to improve the sample saturation by increasing the CO_2-solubility [9]. On the other hand, saturation temperature (T^{sat}) has to be minimized to optimize the saturation step, while complying with the supercritical state, which also contributes to optimize the saturation step due to an advantageous combination of liquid and gaseous properties. The relation between T^{sat} and the speed at which the foam vitrifies (or stabilizes) is a complex issue, certainly overlooked in the literature. Indeed, as foaming is triggered e.g. by an adiabatic pressure *quench*, the effective temperature (T^{ef}) of the plasticized system {polymer + CO_2} is lower than T^{sat} and generally unknown. The vitrification speed is therefore determined, among others, by the interplay between *i)* the evolution of T^{ef} towards room temperature and *ii)* the rising kinetics of the effective glass transition temperature (T_g^{ef}). Once the sample is vitrified ($T_g^{ef} > T^{ef}$), cell growth and coalescence are stopped and one can expect to produce a foam with small cell dimensions.

At the beginning of foaming, another important parameter acts on the foam structure: the pressure drop rate (PDR). The pressure drop rate is typically defined as $\Delta P/\Delta t$, where $\Delta P = P^{sat} - P^{ambient}$ and Δt is the time to return to ambient pressure upon pressure release [19]. Several studies have shown that increasing the pressure drop rate is a relevant way to minimize foam cell size thereby improving the mechanical and thermal properties [19],[20],[21]. This trend has been observed using adapted devices (e.g. PP batch-foaming fitted with a window linked to a camera [22]) allowing observation of the foaming process from the early stages of cell growth. A PDR increase induces an increase of the nuclei formation rate [23]. At a certain stage, nucleation and growth may compete. More precisely, when cell nucleation and growth overlap, the later penalizes the former. When the PDR is increased, the nucleation rate is favored while growth is limited. Increasing the PDR also prevents coalescence by increasing the speed at which the effective glass temperature of the plasticized system {polymer + CO_2} (T_g^{ef}) is overcome (*i.e.* $T^{ef} < T_g^{ef}$) [23],[24]. So, because of its action upon the different foaming steps, the PDR has an influence upon both cell size and cell density [24],[25],[26],[27].

In batch foaming, a *classical* PDR value may be considered as 0.5 MPa.s^{-1} [11]; other PDR values have been studied (30 MPa.s^{-1} [19]; 8.3 MPa.s^{-1} [24]; 0.4 MPa.s^{-1} [28]) by using vessels with a smaller capacity and/or by increasing the outlet pipe diameter to facilitate gas evacuation during foaming. Experimentally, the number of nucleated bubbles per unit volume of unfoamed material (N_0) has been shown to depend linearly upon pressure drop rate in a bi logarithmic scale [24]. A classical PDR (~ 0.5 MPa.s^{-1}) is generally not sufficient to reach a very small pore size as it does not induce a sufficient number of nuclei or do not freeze the structure by a rapid enough thermal quench (consecutive to pressure quench). Simulations of PDR were carried out at an extremely high PDR (250 MPa.s^{-1}) [20],[26]. As a matter of fact, both theoretical and experimental studies show that a PDR increment can increase the cell number density by 1 or 2 decades while cell size decreases by a moderate factor of 2 or 3. Furthermore, most of the systems studied in the literature are probably in a molten state (flowing state), and do not undergo a solid-state (non-flowing) foaming. Thus we may expect a greater influence of the PDR value when the system is solid (solid-state CO_2 foaming).

No work actually states clearly if the mere fact to increase the pressure release rate can increase the cell density (cells.cm^{-3}) up to 10^{15} cell.cm^{-3}, reduce cell size in the nanometer range and simultaneously lower the overall material density (ρ_f) near or below 0.2 g.cm^{-3}. However, in a one-step solid-state batch foaming, appropriate combinations of factors (high PDR, low saturation temperature and introduction of nucleating nano particles) may be beneficial. Such combinations are investigated in this work for neat PMMA and for PMMA/10 wt% MAM blend foams. PMMA and PMMA/10 wt% MAM are CO_2-saturated at temperatures (40 °C and 60 °C) and saturation pressures (20 MPa and 30 MPa) complying with the supercritical state before being foamed (one-step solid-state foaming) over a broad PDR range (from 0.3 MPa.s^{-1} to 30 MPa.s^{-1}). Porous structures are investigated through a quantitative analysis of SEM images at different scales.

2. Materials and Methods

2.1 Materials

Neat poly(methyl methacrylate) (PMMA commercialized as V825T 101 Clear PMMA by Arkema) pellets and neat MAM (M53 grade commercialized by Arkema) triblock copolymer (poly(methyl methacrylate)-co-poly(butyl acrylate)-co-poly(methyl methacrylate)) pellets were supplied by Arkema (Lacq, France). The characteristics of these materials are well documented in literature [12],[18],[29].

2.2 Unfoamed blend compounding

To produce PMMA/10 wt% MAM blend, neat PMMA and MAM pellets were first dried at 80 °C for 4 h in an oven. Then, the blend was compounded by CANOE (Pau, France) using a corotative twin-screw extruder (Labtech, $\emptyset = 26\, mm$, $L/D = 40$) with a temperature profile ranging from 250 °C to 230 °C at a screw speed of 300 rpm. At the end of the extruder line, the blend was pelletized with a continuous cutting machine.

Neat PMMA and PMMA/10 wt% MAM pellets were dried again at 80 °C for 4 h in an oven. Then, transparent tensile test bars (ISO 180/U 80 × 10 × 4 mm^3) of neat PMMA and PMMA/10 wt% MAM were injected with a classical injection-molding device (ENGEL ES 200-45 HL-V). The acrylic polymer and blend were injected at 230 °C at a screw speed of 300 rpm in a mold heated at 90 °C. All injected bulk bars were perfectly transparent.

2.3 One-step batch foaming

PMMA and PMMA/10 wt% MAM were foamed through $scCO_2$-assisted one-step batch process at LCPO and ICMCB laboratories (Bordeaux, France). Varying the PDR over a wide range of values typically requires use of vessels of different capacities and/or outlet pipe diameter [19], [24], [28]. In this study, two vessels were used to vary the PDR by two order of magnitude (Table 1). These two vessels were especially necessary to be able to work with sufficiently large samples; and the bigger-sized vessel could in no way allow reaching 30 $MPa.s^{-1}$.

The samples foamed at « low PDR » (0.3 $MPa.s^{-1}$ and 0.5 $MPa. s^{-1}$) were produced in a high-pressure vessel provided by TOP Industrie (Vaux-le-Pénil, France). The vessel was filled with CO_2 at the desired pressure with a syringe pump Teledyne ISCO model 260 (Lincoln, USA). Because the outlet pipe diameter was fixed, the saturation pressure was set to 20 MPa or 30 MPa to enforce the target PDRs of 0.3 and 0.5 $MPa.s^{-1}$ (values in the range of low PDR). The saturation temperature (40 °C or 60 °C) was controlled with a heating collar. The CO_2 uptake (wt%) was measured in situ using a FTIR (Fourier Transform Infrared) microscope combined to a CO_2 high-pressure cell [9]; $scCO_2$ uptake was found to the same at 20 MPa and 30 MPa (the samples are already fully saturated at 20 MPa at both temperatures) [9]. Therefore, a saturation pressure spread of 10 MPa (20 vs. 30 MPa) had no impact upon the final foam structures. After saturation (during 24 h to ensure full saturation of the samples), the pressure was released with an on/off discharge valve model 910.10.00 provided by TOP Industrie (Vaux-le-Pénil, France).

Samples foamed at higher PDR (4 $MPa.s^{-1}$ and 30 $MPa.s^{-1}$) were produced in a smaller-sized vessel (0.057 L) provided by Swagelok (Lyon, France). In this vessel, the PDR could be varied by adapting the geometry of the vessel (outlet pipe diameter; Table 1). After saturation (24 h), the pressure was released with an on/off discharge valve model SS-AFSS12 provided by Swagelok (Lyon, France).

Table 1. *Batch set-up dimensions versus PDR*

PDR ($MPa.s^{-1}$)	Vessel capacity (cm^3)	Outlet pipe internal diameter (cm)
0.3	300	0.2
0.5	300	0.2
4	57	2.36
30	57	13.51

2.4 Characterization techniques

i. Water pycnometer

Unfoamed materials density (ρ_s) and foams density (ρ_f) were determined with a water pycnometer following the water displacement method, based on Archimedes' principle. Three measurements were performed for each sample.

ii. Electron microscopy observations and image analysis

- PMMA/10 wt% MAM dense precursor blend: TEM observations

The structure of the solid PMMA/10 wt% MAM blend precursor was observed through TEM. Before observation, the solid blend was cut into a cryo-ultramicrotome LEICA EM UC7-FC7 (Wetzlar, Germany) at - 75 °C with a diamond knife at the Bordeaux Imaging Center (BIC, Bordeaux, France). The thin cuts (80 – 100 nm thick) were collected on copper grids before being contrasted with an aqueous solution containing 2 wt% phosphotungstic acid (PTA) + 2 wt% benzyl alcohol at ambient temperature. As reported in the literature, PTA preferentially colors at ambient temperature the CO_2-philic PBA soft block (in black or dark grey on TEM images) over the PMMA more rigid block (white or light grey on TEM images) [6],[11]. Benzyl alcohol acts as a dyeing assistant and helps PTA coloration of PBA. TEM observations were performed at 80 kV at magnifications ranging from X15 000 to X200 000 (Figure 1.A). The exhibited nanostructures can be qualified as micellar objects or micelle-like objects.

- Image analysis of TEM micrographs

TEM images captured at several magnifications were analyzed in order to quantify the micellar objects and determine automatically their characteristics. To further improve the level of contrast permitted by staining (Figure 1.A) and facilitate the subsequent segmentation of the micellar objects (Figure 1.C), we adopted a multiscale (multiresolution) description of electronic images (thereafter electronic images are denoted by $u(\mathbf{x})$, where u is the grey level intensity function at every pixel $\mathbf{x} = (x_1, x_2)$). Descriptions that depend on scale (or resolution) may be computed in several ways. We retained the so-called *scale-space filtering* [30],[31]. In this approach, the original image $u(\mathbf{x})$ (Figure 1.A) is embedded in a family of images $u(\mathbf{x}, t)$ at coarser resolutions (larger scale levels) *cf* e.g. Figure 1.B. Such family of images $u(\mathbf{x}, t)$ is obtained by filtering $u(\mathbf{x})$ over increasing scales whose size is parametrized by the increasing time t of a diffusion equation [32]. The resulting family of images $u(\mathbf{x}, t)$ produced by varying continuously the scale-space parameter t is called the scale-space image.

Because information content decreases towards higher levels (at coarser resolutions), edges or boundaries (the zero-crossings of the Laplacian of the image) are moved when sweeping out the scale-space image. In this sense, we can say that the material is virtually reconstructed as illustrated in Figure 1.B. With this multiscale (multiresolution) description, we could detect more readily image features at different resolutions (e.g. Figure 1.B). In this approach, the key point is that images have by nature a hierarchical organization composed of a small number of levels or scales [33]. There is a natural range of resolutions, in other words intervals of the scale-space parameter t, corresponding to each of these *semantic* levels of description, where the interphases and/or interfaces of interest are better perceived and even reconstructed (Figure 1.B). As illustrated in Figure 1.B, the reconstructed image tends to a piecewise constant solution representing a simplified image with sharper boundaries, permitting to easily segment interphases e.g. by direct thresholding without recourse to any complex treatment of image analysis. To achieve this, we followed the route paved by Perona and Malik [34]. We relied on a nonlinear scale space, where blurring is locally adaptive to image data: the diffusion process (blurring) mainly takes place in *flat* regions (PMMA matrix) where the magnitude of the gradient $\left(\boldsymbol{\nabla}(\,)=\left(\frac{\partial()}{\partial_{x_1}},\frac{\partial()}{\partial_{x_2}}\right)\right)$ of the grey level intensity $||\boldsymbol{\nabla}u||$ is low. On the other hand, blurring does not affect region boundaries (micellar object boundaries), where $||\boldsymbol{\nabla}u||$ is larger. Furthermore, in the neighborhood of marked discontinuities (boundaries), where $||\boldsymbol{\nabla}u||$ is high across the level curve of the intensity u, the diffusion process is running locally backwards, normal to the isoline of u *i.e.* normal to the boundary, which is thereby steepened (contrast enhancement; Figure 1.B).

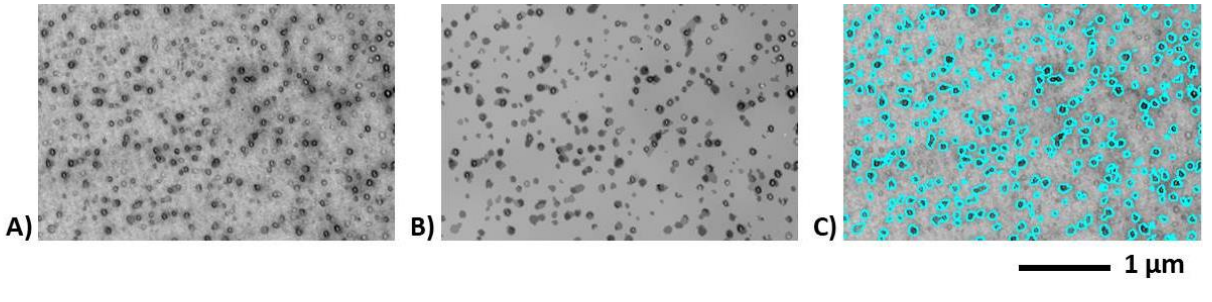

Figure 1. *Illustration of the segmentation of micellar objects.* ***A)*** *Local close up in a TEM micrograph (X20 000) showing dispersed micellar objects formed by MAM tri-block copolymers in a 90/10 PMMA/MAM solid blend precursor.* ***B)*** *Enhanced image after applying to Figure 1.A a nonlinear directional diffusive filter. In this filtering procedure, Gaussian blurring applies selectively to flat regions, which are dissipated, while the boundaries and the contrast of the nanostructures of interest are clearly enhanced.* ***C)*** *Binarized (0 -1) counterpart of the grey level image in Figure 1.B. In this display, the contours of the segmented nanostructures (labeled with a 1 value) are displayed in cyan, superimposed upon the original image (Figure 1.A) rather than leaving in transparency the 0-valued background matrix.*

Before segmentation, the filtered image $u(\mathbf{x},t)$ was, when necessary, corrected for shading (uneven background matrix). Touching/overlapping micellar objects were automatically separated before size and shape measurements. To do so, we assumed, as others e.g. Canseco et al. [35], a systematic region growing approach [36]. After disconnection of overlapping objects, the binary image (e.g. Figure 1.C) was perfectly suited to the automatic measurement of the object size statistical distribution (Figure 2). The effective diameter D of every micellar object was derived from the object perimeter P measured by integrating for all affine lines in the plane the Euler-Poincaré characteristic of the intersection of the line with the object [37].

The rather large distribution of the micellar objects diameter (Figure 2) suggests that the system is not at equilibrium (a liquid micellar system would show a mono modal distribution). The non-equilibrium state comes from several reasons: *i)* the macromolecular nature and chain polydispersity of MAM, *ii)* the high viscosity and temperature quenching of the blend during the extrusion stage, where the blend is sheared and cooled at the end of the die.

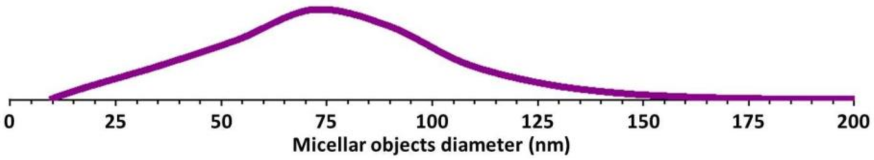

Figure 2. *Nanostructure size distribution automatically determined from segmented objects (Figure 1.C). In this display, the finite size interval bins of the original discrete frequency histogram of the object diameters are schematically represented as a continuous distribution of the object percentile as a function of cell size. The vertical full scale is set to the highest nanostructure percentile of the original frequency histogram.*

Some of the characteristics derived from the nanostructure size distribution of the 10 wt% MAM solid precursor (Figure 2) are listed in Table 2, namely the nanostructure number density N_s (objects.cm^{-3}), the nanostructure average diameter $\overline{D}_s$ and the aggregation number $N_{aggregation}$ (number of copolymer molecules per nanostructure). Assuming that all the copolymer lies inside the micellar objects, an upper bound of the aggregation number was estimated as:

$$N_{aggregation} = \frac{w\, N_a\, \rho_s}{M_n\, N_s} \qquad Eq. 1$$

where w is the amount of copolymer (wt%) and $N_a = 6.02\ 10^{23}\ mol^{-1}$ the Avogadro's number, M_n number average molar mass.

Table 2. *Characteristics of PMMA/10 wt% MAM solid precursors.*

Solid sample ID	Nanostructure density N_s (objects.cm^{-3})	Nanostructure average diameter $\overline{D}_s$ (nm)	Density of the solid blend ρ_s (g.cm^{-3})	Predicted aggregation number $N_{aggregation}$
PMMA/10 wt% MAM	$2.4\ 10^{14} \pm 0.2\ 10^{14}$	68 ± 8	1.19 ± 0.07	3700

Compared to the literature, the micellar objects average diameter is consistent with previous determinations. Nevertheless, the number density of 2.4 10^{14} objects.cm^{-3} seems an insufficient nucleating density to provide true nano foams (requiring an order of magnitude of 10^{15} to 10^{16} objects.cm^{-3} [38]).

- PMMA and PMMA/10 wt% MAM foams: SEM observation

PMMA and PMMA/10 wt% MAM foam structures were observed on micrographs acquired with an environmental scanning electron microscope (E-SEM), a Quanta FEG 250 from FEI/ThermoFisher. Before observation, the foamed samples were frozen in liquid nitrogen, fractured (perpendicularly to the height) and sputter-coated with a thin layer of gold. All samples were imaged at low acceleration voltage (< 5 keV) and current (a few pA to a few tens of pA) (not to damage the foam structure with the primary electron beam). Images were formed by collecting the secondary electron (SE) emission. In this situation, contrast is said topographical and is made of three contributions: the inclination contrast, the shading contrast and the ridge contrast. Each sample was imaged at several magnifications (from X100 to X100 000). Figure 3.A illustrates over a local area the structure of a foam sample produced from the 90/10 PMMA/MAM blend at a saturation temperature of 60 °C, and a pressure drop rate of 0.3 MPa.s^{-1}.

- Image analysis of SEM image

In micrographs formed in secondary electron mode, both shading and ridge contrasts promote darker foam cells than the polymeric background solid lattice. Yet, dependence of the secondary emission upon the incident angle of the primary electron beam (inclination contrast) may work locally *the other way around*, depending on the local geometry of the sample. Thus, there is again a need to further increase contrast in order to develop a sound automatic method for the determination of the cell size distribution. We took again advantage of the nonlinear directional diffusive filter described earlier to reach a suitable level of (enhanced) contrast. After this contrast augmentation, the segmentation of smooth and darker foam cells standing out from a brighter solid lattice could be accomplished via a simple threshold. The object sets segmented thereby, like the one illustrated in Figure 3.B, were suited for the automatic determination of the object diameter statistical distribution (Figure 4), the diameter of every object being derived from measurement of its perimeter.

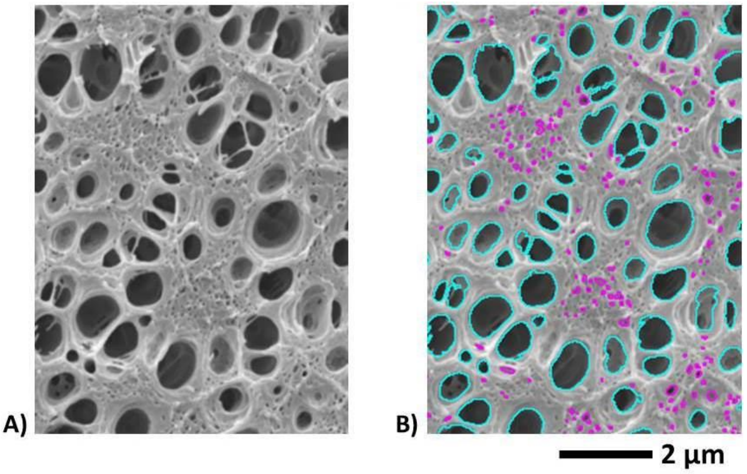

Figure 3. A) *Cellular structure produced from a PMMA/10 wt% MAM blend saturated with* $scCO_2$ *at 60 °C and then foamed in one-step batch-foaming with a pressure release rate of 0.3* $MPa.s^{-1}$. ***B)*** *The segmented object set (cell set) includes inter skeletal pores (in cyan) and intra skeletal pores (in magenta).*

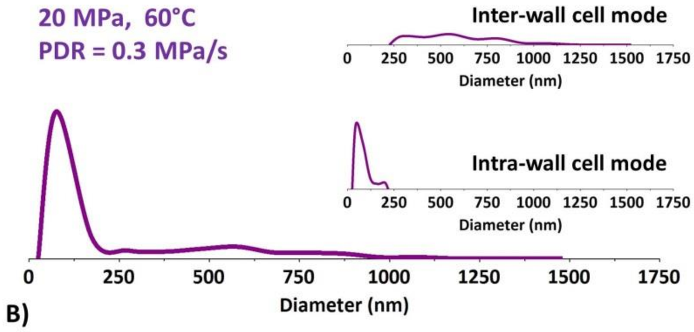

Figure 4. *Cell size distribution of the foam sample locally illustrated in Figure 3. The vertical full scale is set to the highest cell % of the frequency histogram. The foam sample shows two scales of porosity (Figure 3). The intra- and inter-wall cell size modes of the global (bimodal) size distribution (lower curve) were further specified by filtering the segmented object set (cell set). Filtering consisted in removing those objects from an object set whose filter size attribute (e.g. object diameter or area) fell outside a specified range. The chosen object size attribute threshold value was that one which partitioned unequivocally the cell set in two classes of porosity: small-sized intra-wall cells (in magenta) versus much larger inter-wall cells (in cyan) (Figure 3).*

Several important characteristics were derived from the cell size distributions including the cell number density (N_{cell}, cell.cm^{-3}), the cell nucleation density (N_0, nuclei.cm^{-3}) and the mean cell size ($\overline{D}_{cell}$). The cell number density in the porous material (N_{cell}) was calculated using Equation (2).

$$N_{cell} = \left(\frac{m}{A}\right)^{3/2} \qquad Eq.2$$

where m is the number of cells segmented in an image (collection of images) and A is the area of the digital image (collection of digital images) in cm^2.

The cell nucleation density in the foamed material (N_0) represents the number of pores formed per cubic centimeter of the unfoamed dense blend precursor making implicitly the hypothesis that there is no coalescence during the stabilization of the foam structure. N_0 was calculated using Equation (3).

$$N_0 = N_{cell} \times \frac{\rho_s}{\rho_f} \qquad Eq. 3$$

N_0 can be paralleled to the micellar objects density (N_s) measured in the dense blend precursor. Those values should be ideally as close as possible.

SEM images at different scales and their quantitative analysis revealed two scales of pores in several of the foams produced from the 90/10 PMMA/MAM blend *cf* e.g. Figure 3 namely, inter-skeletal micropores (voids separated by cell walls as defined by Kaneko et al. in a general review on solid porous materials [39]) and intra-skeletal much smaller nanopores, located inside the cell walls. In this instance three average diameters were calculated: $\overline{D}_{cell}$ the global mean cell diameter, $\overline{D}_{inter-wall\ cell}$ the inter skeletal pore mean diameter and $\overline{D}_{intra-wall\ cell}$ the intra skeletal pore mean diameter. When intra skeletal pores are present, $\overline{D}_{cell}$ contains information (weighted average) from $\overline{D}_{inter-wall\ cell}$ and $\overline{D}_{intra-wall\ cell}$; while $\overline{D}_{cell} \equiv \overline{D}_{inter-wall\ cell}$ when there is no intra skeletal pores. The size distributions (including the inter wall and intra wall cell modes in case of bimodal distribution *cf* e.g. Figure 4) of all studied foam samples are provided and discussed in the next section.

3. Results and discussion

3.1 Porous structures after one-step batch foaming (SEM Imaging)

This section (3.1) describes qualitatively the different morphologies observed on SEM micrographs and outlines general trends. The next section (3.2) deals with the quantification of the structural information contained in the SEM micrographs.

3.1.1 PMMA foam structures

Neat PMMA samples were foamed at PDR ranging from 0.3 MPa.s^{-1} to 30 MPa.s^{-1}. The influence of the saturation temperature and the PDR on the structure of the final PMMA foams is illustrated in Figure 5.

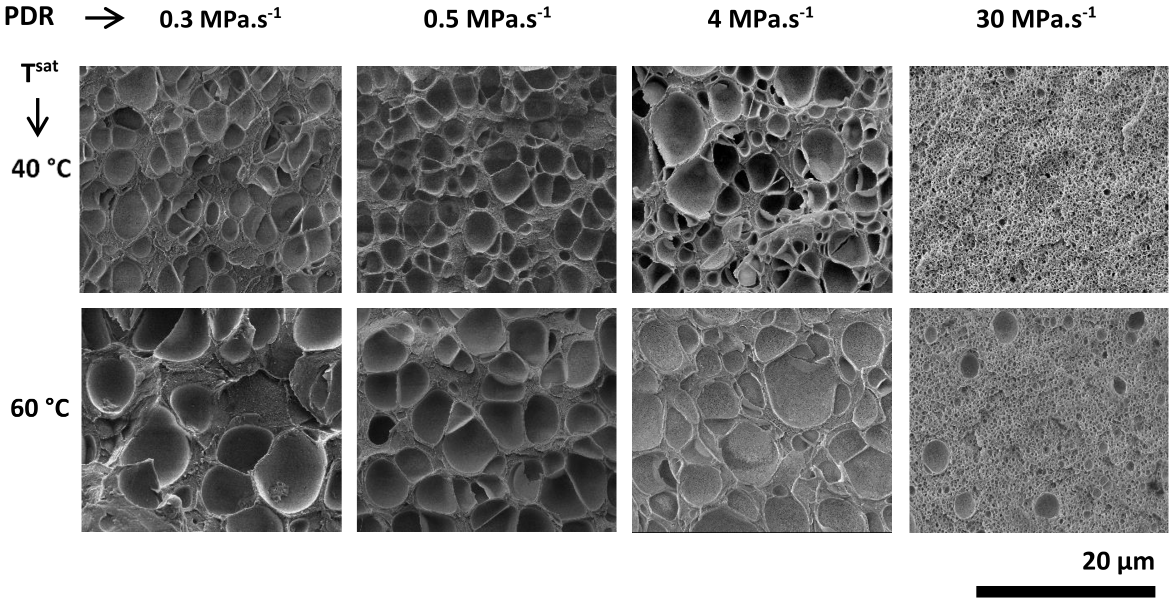

Figure 5. *SEM images of neat PMMA saturated at either 40 °C or 60 °C (P^{sat} = 20 MPa or 30 MPa) at a PDR ranging from 0.3 MPa.s^{-1} to 30 MPa.s^{-1} (in a one-step batch foaming process)*

At a fixed saturation temperature (either 40 °C or 60 °C), PMMA foamed at low to moderate PDR (*i.e.* between 0.3 MPa.s^{-1} and 4 MPa.s^{-1}) are comparable. In other words, at a given temperature, the foam cell size is not significantly influenced by the PDR value (Figure 5). Although the foam cells of the samples scCO$_2$-saturated at 40°C appear a little smaller than those of the samples saturated at 60 °C, the cell dimension remains in the same order of magnitude at low to moderate PDR.

Only a high PDR of 30 MPa.s^{-1} induces a true change towards much smaller cells. Moreover, the sample foamed at 30 MPa.s^{-1} after a saturation at 60 °C contains two types of porosities, while the sample saturated at 40 °C is monomodal (only small pores).

As a first global summary for PMMA foams, the cell dimension is mainly governed by the saturation temperature at low to moderate PDR, while cell dimension is principally governed by PDR at 30 MPa.s^{-1}.

3.1.2 PMMA/10 wt% MAM foam structures

PMMA/10 wt% MAM blend samples were foamed in the same conditions as for neat PMMA (Figure 6). As observed in the case of PMMA, saturation temperature and PDR are competing to determine the PMMA/10 wt% MAM final foam structure.

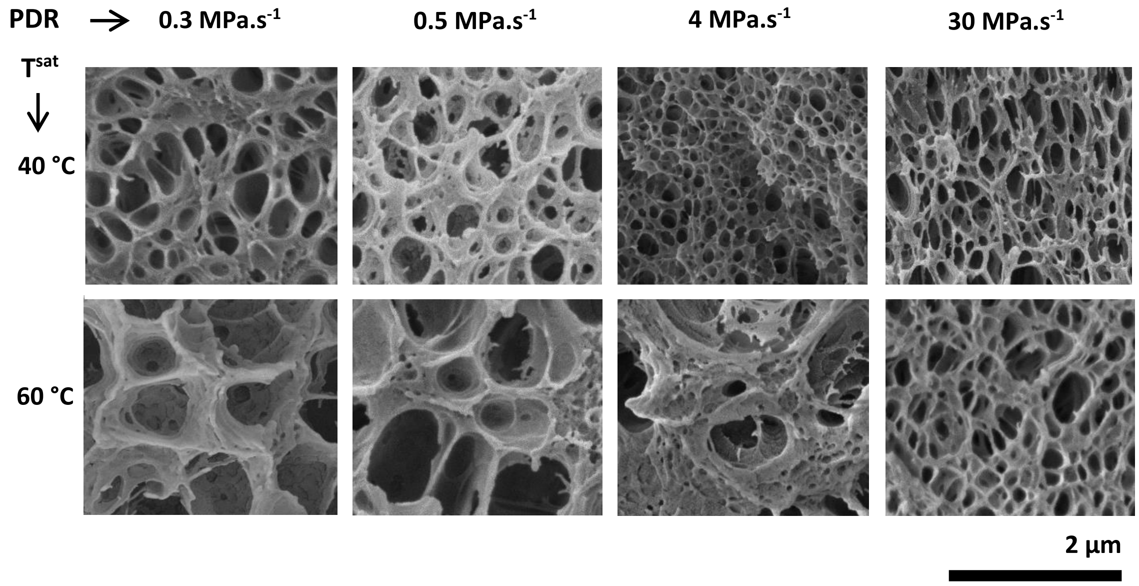

Figure 6. *SEM images of PMMA/10 wt% MAM blend foamed after saturation at 40 °C and 60 °C (P^{sat} = 20 MPa or 30 MPa) using a PDR ranging from 0.3 $MPa.s^{-1}$ to 30 $MPa.s^{-1}$ (in one-step batch foaming process).*

At fixed temperature, PMMA/10 wt% MAM samples foamed at low PDR (0.3 to 0.5 $MPa.s^{-1}$) are not significantly affected by the PDR value (Figure 6). But, over that PDR range, the $scCO_2$ saturation temperature plays a more important role upon the inter-wall cell size: the lower the saturation temperature is, the smaller is the inter-wall cell size.

At the moderate PDR of 4 $MPa.s^{-1}$, both the saturation temperature and the PDR impact cell size. At 40 °C, the 4 $MPa.s^{-1}$ PDR leads to a much smaller cell size than at lower PDR, while at 60 °C, the inter-wall cell size is still comparable to that observed at lower PDR.

Samples foamed at the highest PDR (30 $MPa.s^{-1}$) contain small cells of the same size independently of the saturation temperature, which no longer impacts the final foam structure.

Whatever the thermodynamic conditions are (P^{sat}, T^{sat}, t^{sat}, PDR), the addition of MAM in PMMA systematically induces smaller porosity dimensions than in neat PMMA foams (note that Figure 6 is shown at a scale ten times smaller than in Figure 5). This trend of cell size reduction, already reported in the literature, can be explained in terms of CO_2 local concentration, heterogeneous nucleation and increased cell density [7],[8],[9],[10],[11].

As a first conclusion, in a one-step solid-state foaming, if the material formulation always influences the foam structure, a high PDR acts as a supplementary beneficial variable to efficiently achieve the targeted cell size reduction as observed by SEM imaging.

3.2 Structural quantification by image analysis

This section presents the structural quantification of PMMA and PMMA/10 wt% MAM foams by image analysis. For each foam sample, several SEM images captured at various magnifications were automatically segmented according to the procedure presented in *Section 2.4* in order to determine a representative cell size statistical distribution *cf* e.g. Figure 7 for neat PMMA.

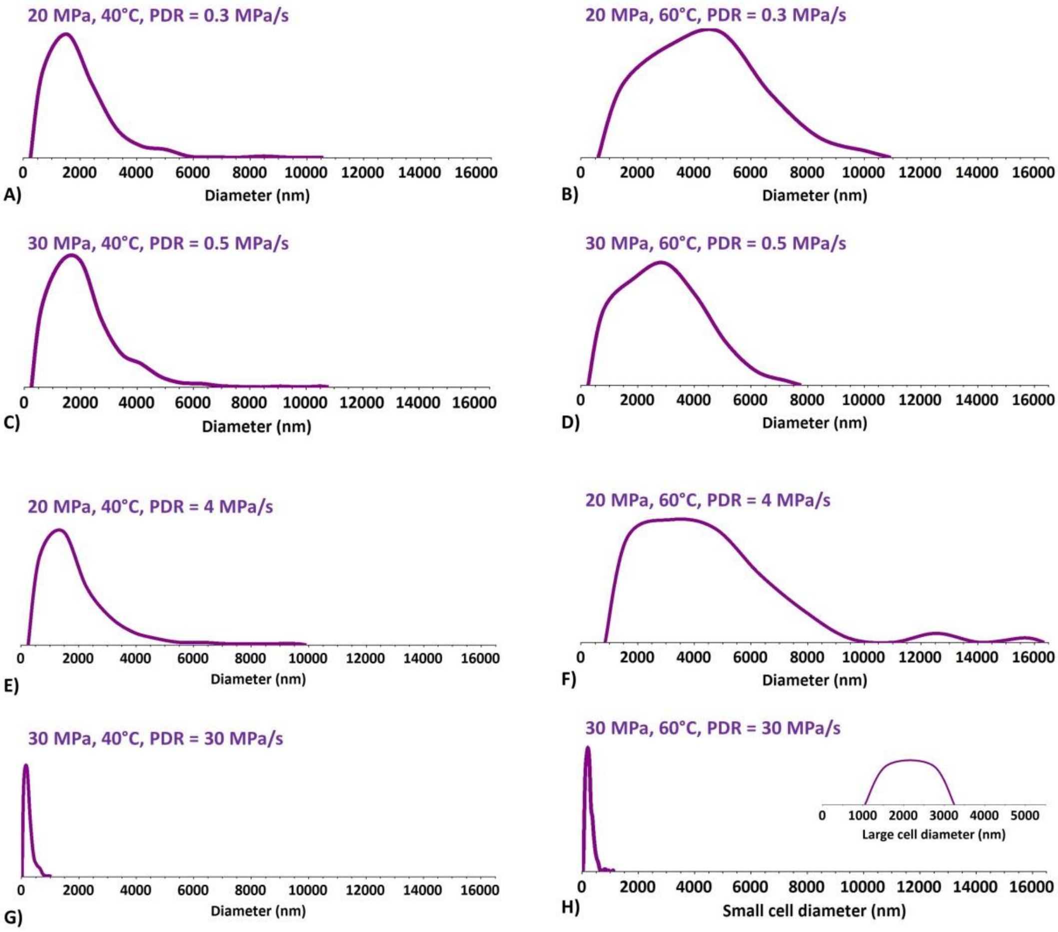

Figure 7. *Cell size distributions of the foams produced from neat PMMA. As discussed further below, the sample saturated at 60°C and foamed using a PDR of 30 MPa.s*$^{-1}$ *is bimodal (see Figure 5). The two modes (small vs. large size) of the cell size distribution were specified relying on a filtering procedure similar to that described in the legend of Figure 4.*

Morphological characteristics of the foams from neat PMMA including average cell size, cell number density and nuclei number density were derived from the calculated cell size distributions in Figure 7. These characteristics are compiled in Table 3.

Table 3. *Neat PMMA foams morphological characteristics determined by quantitative image analysis.*

PMMA Foam	Foam density ρ_f (g.cm^{-3})	Average cell size $\overline{D}_{cell}$ (nm)	Cell density N_{Cell} (cells.cm^{-3})	Nuclei density $N_0 = N_{cell} \times \rho_s / \rho_f$ (nuclei.cm^{-3})
P^{sat} = 20 MPa T^{sat} = 40 °C PDR = **0.3 MPa.s^{-1}**	0.78 ± 0.05	1900 ± 46	$3.2 \times 10^{10} \pm 0.6 \times 10^{10}$	$4.8 \times 10^{10} \pm 1.2 \times 10^{10}$

P^{sat} = 20 MPa T^{sat} = 60 °C PDR = **0.3 MPa.s^{-1}**	0.81 ± 0.03	4340 ± 119	$4.2 \times 10^{9} \pm 0.3 \times 10^{9}$	$6.1 \times 10^{9} \pm 0.7 \times 10^{9}$
P^{sat} = 30 MPa T^{sat} = 40 °C PDR = **0.5 MPa.s^{-1}**	0.76 ± 0.09	2070 ± 43	$3.3 \times 10^{10} \pm 0.1 \times 10^{10}$	$5.1 \times 10^{10} \pm 0.8 \times 10^{10}$
P^{sat} = 30 MPa T^{sat} = 60 °C PDR = **0.5 MPa.s^{-1}**	0.6 ± 0.02	2892 ± 60	$1.6 \times 10^{10} \pm 0.2 \times 10^{10}$	$3.1 \times 10^{10} \pm 0.5 \times 10^{10}$
P^{sat} = 20 MPa T^{sat} = 40 °C PDR = **4 MPa.s^{-1}**	0.64 ± 0.01	1867 ± 61	$5.9 \times 10^{10} \pm 2.0 \times 10^{10}$	$1.1 \times 10^{11} \pm 0.4 \times 10^{11}$
P^{sat} = 20 MPa T^{sat} = 60 °C PDR = **4 MPa.s^{-1}**	0.52 ± 0.003	4373 ± 299	$4.9 \times 10^{9} \pm 2.0 \times 10^{9}$	$1.1 \times 10^{10} \pm 0.5 \times 10^{10}$
P^{sat} = 30 MPa T^{sat} = 40 °C PDR = **30 MPa.s^{-1}**	0.53 ± 0.003	231 ± 10	$2.1 \times 10^{13} \pm 0.2 \times 10^{13}$	$4.6 \times 10^{13} \pm 0.5 \times 10^{13}$
P^{sat} = 30 MPa T^{sat} = 60 °C PDR = **30 MPa.s^{-1}**	0.6 ± 0.01	250 ± 8	$1.8 \times 10^{13} \pm 0.1 \times 10^{13}$	$3.5 \times 10^{13} \pm 0.1 \times 10^{13}$

The PMMA foams imaged in Figure 5 are essentially « homogeneous » i.e. their cell size distributions (Figure 7) are monomodal, apart from one sample saturated at 60 °C and foamed at 30 MPa.s^{-1}. This sample shows two porosity populations: numerous small-sized cells and far less numerous much larger cells, both dispersed in the solid lattice. For this foam, the mean cell size listed in Table 3 (last row) is the weighted average of the two populations. Aided by the marked difference in size of the two populations, the average size and number density of the larger cells were assessed (Figure 8) by applying a connected filter (an opening by reconstruction) to the segmented/binarized image. More precisely, a large-sized morphological erosion followed by a geodesic dilation of infinite size, was used to discard the small cell population (Figure 8.B). This discrete (in number) large cell population shall be paralleled to the systematic large cells observed at 60 °C at lower PDR (0.3 to 4 MPa.s^{-1}). In other words, in the case of homogenous nucleation, a PDR as high as 30 MPa.s^{-1} is not high enough to suppress totally the impact of temperature upon the final foam structure. As mentioned earlier, the situation is different in the case of heterogeneous nucleation, where the saturation temperature no longer influences the final foam structure, which is only controlled by such a high PDR (30 MPa.s^{-1}).

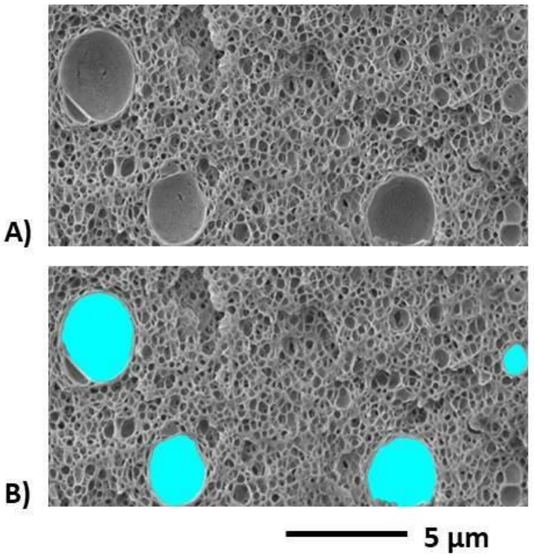

PMMA foam	Larger cell average size $\bar{D}_{large\ cell}$ (nm)	Large cell density (cells.cm^{-3})
P^{sat} = 30 MPa T^{sat} = 60°C PDR = **30 MPa.s^{-1}**	2188 ± 215	$3.2 \times 10^9 \pm 0.3 \times 10^9$

Figure 8. *Local illustration of the segmentation (binarization) of the large cell population of the PMMA foam saturated at 60 °C and foamed at a high PDR of 30 MPa.s^{-1}.*

Quite interestingly, PMMA/10 wt% MAM foams reveal a cell size bimodality in the majority of the samples up to a PDR of 4 MPa.s^{-1}. The cell size distributions (Figure 9) and associated morphological characteristics (Table 4) were first determined considering all cells with no distinction.

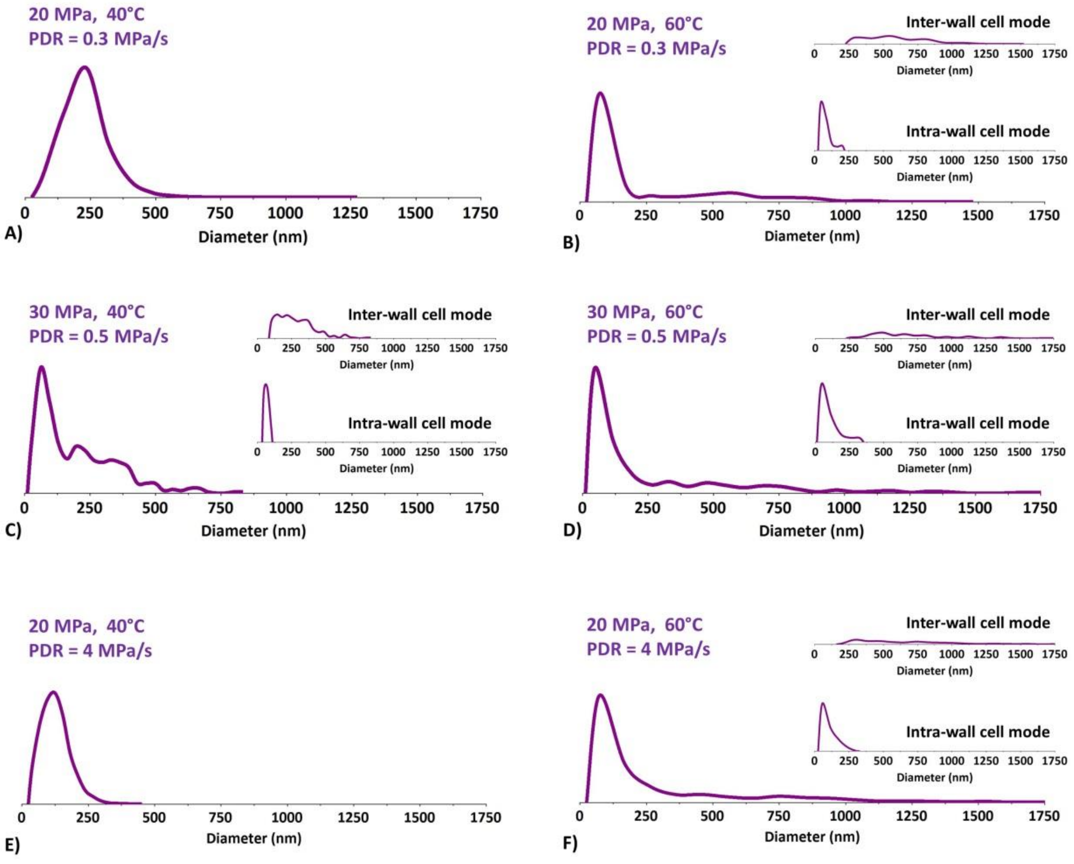

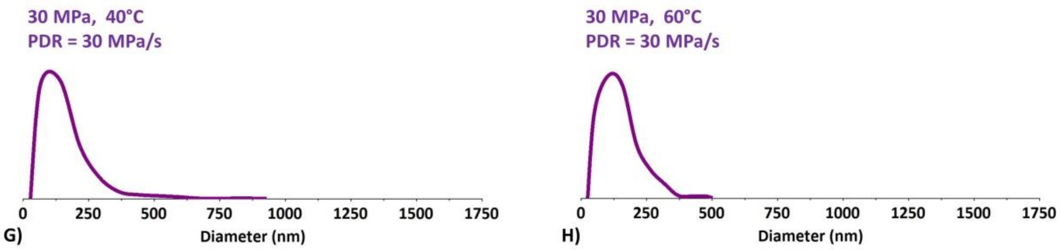

Figure 9. *Cell size distributions of the foams produced from 90/10 PMMA/MAM blends. Refer to Figure 4 for a more complete legend.*

Then, for bimodal samples, small porosities, referred to as intra skeletal pores, localized within locally thicker struts and inter-cell walls were distinguished from inter skeletal pores. Using the image analysis procedures described in *Section 2.4 cf* e.g. Figure 3.B, the two modes of the global cell size distributions were determined (Figure 9). The mean diameter of each cell mode is given in Table 5 along with the inter-wall cell fraction (%).

Table 4. *PMMA 10 wt% MAM foams morphological characteristics determined by quantitative image analysis.*

PMMA/10 wt% MAM Foam	Foam density ρ_f (g.cm^{-3})	Average cell size $\overline{D}_{cell}$ (nm)	Cell density N_{Cell} (cells.cm^{-3})	Nuclei density $N_0 = N_{cell} \times \rho_s/\rho_f$ (nuclei.cm^{-3})	Number of modes
P^{sat} = 20 MPa T^{sat} = 40 °C PDR = **0.3 MPa.s^{-1}**	0.85 ± 0.002	228 ± 3	$1.2 \times 10^{13} \pm 0.1 \times 10^{13}$	$1.7 \times 10^{13} \pm 0.2 \times 10^{13}$	Very slightly bimodal*
P^{sat} = 20 MPa T^{sat} = 60 °C PDR = **0.3 MPa.s^{-1}**	0.67 ± 0.01	206 ± 5	$1.0 \times 10^{13} \pm 0.2 \times 10^{13}$	$1.8 \times 10^{13} \pm 0.5 \times 10^{13}$	**Bimodal**
P^{sat} = 30 MPa T^{sat} = 40 °C PDR = **0.5 MPa.s^{-1}**	0.66 ± 0.01	193 ± 4	$3.6 \times 10^{13} \pm 0.2 \times 10^{13}$	$6.5 \times 10^{13} \pm 0.8 \times 10^{13}$	**Bimodal**
P^{sat} = 30 MPa T^{sat} = 60 °C PDR = **0.5 MPa.s^{-1}**	0.53 ± 0.01	239 ± 57	$1.5 \times 10^{13} \pm 0.5 \times 10^{13}$	$3.4 \times 10^{13} \pm 1.4 \times 10^{13}$	**Bimodal**
P^{sat} = 20 MPa T^{sat} = 40 °C PDR = **4 MPa.s^{-1}**	0.59 ± 0.01	126 ± 4	$5.2 \times 10^{13} \pm 2.1 \times 10^{13}$	$1.0 \times 10^{14} \pm 0.5 \times 10^{14}$	Monomodal
P^{sat} = 20 MPa T^{sat} = 60 °C PDR = **4 MPa.s^{-1}**	0.52 ± 0.02	260 ± 20	$1.4 \times 10^{13} \pm 0.4 \times 10^{13}$	$3.2 \times 10^{13} \pm 1.2 \times 10^{13}$	**Bimodal**
P^{sat} = 30 MPa T^{sat} = 40 °C PDR = **30 MPa.s^{-1}**	0.52 ± 0.004	152 ± 6	$7.9 \times 10^{13} \pm 0.6 \times 10^{13}$	$1.8 \times 10^{14} \pm 0.3 \times 10^{14}$	Monomodal
P^{sat} = 30 MPa T^{sat} = 60 °C PDR = **30 MPa.s^{-1}**	0.51 ± 0.001	143 ± 3	$9.3 \times 10^{13} \pm 1.3 \times 10^{13}$	$2.2 \times 10^{14} \pm 0.4 \times 10^{14}$	Monomodal

*Foam samples produced at 40 °C and at the lowest pressure drop (0.3 MPa.s^{-1}) were very locally typified by thick walls and struts showing a discrete nano-scaled porosity. Such local areas being so few, those samples were considered as (essentially) monomodal.

Table 5. *Some of the foams produced from 90/10 PMMA/MAM solid blend showed clearly two scales of porosity i.e. nano-sized intra-wall cells versus micro-sized inter-wall cells. The inter-wall cell fraction was calculated as the inter-cell number to total cell number.*

PMMA/10 wt% MAM Foam	Average intra-wall cell size $\overline{D}_{intra-wall\ cell}$ (nm)	Average inter-wall cell size $\overline{D}_{inter-wall\ cell}$ (nm)	Inter-wall cell fraction (%)

P^{sat} = 20 MPa T^{sat} = 60 °C PDR = **0.3 MPa.s^{-1}**	76 ± 4	572 ± 6	24 ± 1
P^{sat} = 30 MPa T^{sat} = 40 °C PDR = **0.5 MPa.s^{-1}**	65 ± 5	277 ± 3	60 ± 1
P^{sat} = 30 MPa T^{sat} = 60 °C PDR = **0.5 MPa.s^{-1}**	95 ± 4	671 ± 18	25 ± 9
P^{sat} = 20 MPa T^{sat} = 60 °C PDR = **4 MPa.s^{-1}**	95 ± 4	658 ± 21	29 ± 2

To the authors' knowledge, this is the first time such a double porosity is mentioned and quantified in PMMA/MAM acrylic micro-nano foams. The intra-skeletal pores appear as a reproducible sub population of nano pores with an average diameter ranging from 65 to 95 nm (Table 5). One candidate explanation may be that bimodal foams are formed by a twofold separation process *i.e.* two successive nucleation growth (N-G) processes. The first to occur is the expected or « classical » N-G process. The second N-G process would occur during a subsequent second foaming step inside still CO_2-filled MAM micellar objects within the walls. In other words, residual CO_2 in micellar objects enables a second foaming and therefore, an intra skeletal true nano porosity. The reason for this may be that the PDR at which the pressure is released is actually uncontrolled and shall be regarded as an average PDR. To be more precise, a PDR of 0.5 MPa.s^{-1} shall read as *an average* PDR (APDR) of 0.5 MPa.s^{-1}. Using an APDR of 0.5 MPa.s^{-1}, Pinto et al. [40] have measured the evolution of the instantaneous pressure and temperature during the depressurization stage (see Figure 8 of their paper). During the early stages (in the first seconds) of the depressurization, the system temperature stays around T^{sat}, while pressure decreases abruptly at an instantaneous rate far higher (by almost one order of magnitude) than the APDR (Figure 10). These early stages, typified by a high temperature and a high instantaneous PDR, originate the aforementioned first expected N-G process (whereby MAM nanostructures act as effective nucleants) responsible for the inter-skeletal cell population. After these early stages, the depressurization stage continues with a regular drop of the vessel temperature (down to values below RT), while instantaneous pressure decreases (towards ambient pressure) at a much slower instantaneous rate, say one order of magnitude lower than the APDR (Figure 10). Where the first N-G process occurred, the effective glass transition temperature of the PMMA matrix T_g^{ef} has rapidly raised (due to CO_2 release during the first N-G process) and the system is the therefore locally vitrified. The second N-G process responsible for the intra-skeletal nano-cell population is going to develop independently of the first N-G process, in local areas where residual CO_2 is still available. The slow instantaneous PDR, the effective temperature and the effective glass temperature are less favorable. Cell growth is thus minimized. Due to the very low effective (instantaneous) PDR (Figure 10), only MAM nanostructures still concentrating the blowing agent can nucleate [8]. Recall that using scCO$_2$ Arora et al. [41] produced bimodal foams from a polystyrene precursor by reducing the pressure in stages. The marked slope change in instantaneous pressure decrease that typifies the pressure release in our study (*i.e.* steep decrease during the early stage of the depressurization followed by an almost asymptotic behavior down to ambient pressure (Figure 10)) shall be paralleled to a pressure reduction in stages.

As always, the depressurization step most likely induces local temperature and pressure gradients. The information recorded by *punctual* pressure and temperature sensors, as schematically represented in Figure 10, is by definition sensitive to such gradients. Yet, the main trends discussed in this work i.e. *i)* a first regime typified by a nearly constant effective temperature $T^{ef}(t)$ and an instantaneous PDR $\frac{dP(t)}{dt}$ one order of magnitude higher than the APDR and *ii)* a second regime characterized by a regular drop of $T^{ef}(t)$ and a pressure decrease $\frac{dP(t)}{dt}$ one order of magnitude smaller than the APDR, remain true at the sample-scale, irrespective of local gradients.

As the APDR is increased, the first N-G process implies more and more MAM nanostructures so that ultimately (at 30 MPa.s^{-1} in our work) there is no MAM nucleants left for a second N-G process.

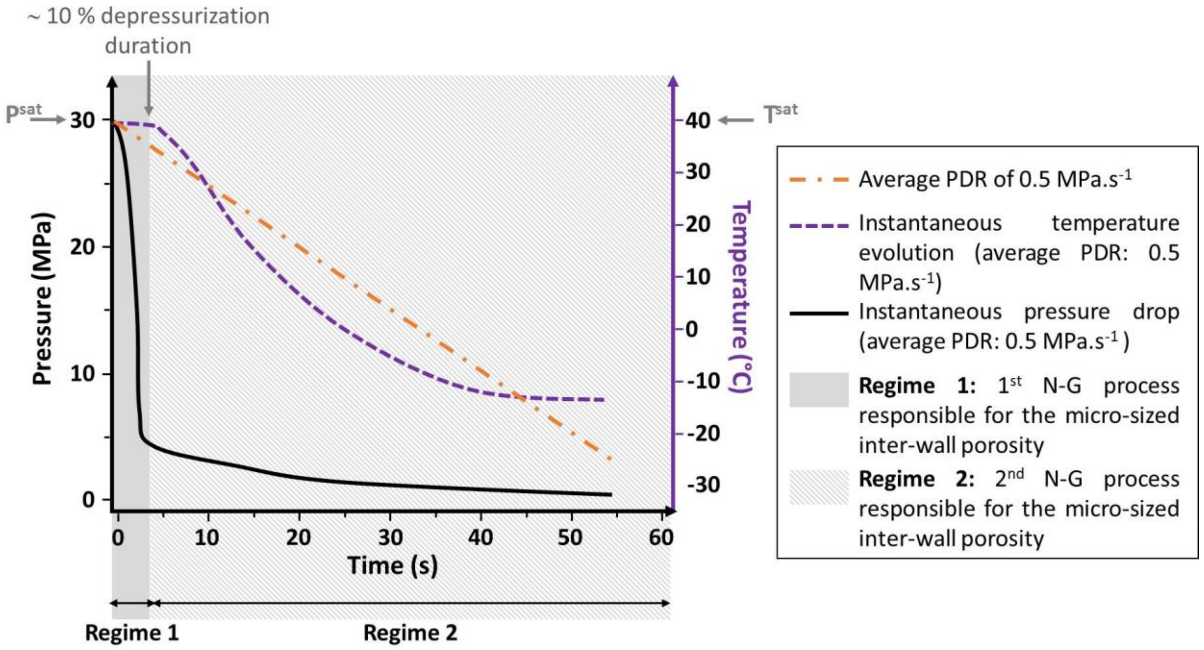

Figure 10. *Schematic representation of the instantaneous (true) pressure and temperature evolution during a depressurization process of average PDR (APDR) equal to 0.5 MP.s^{-1}. Modified from original experimental work by Pinto et al. [40] using the same high-pressure vessel and the same operating conditions than in this study.*

In our view, the bimodal blend foams observed in this study essentially when using an average PDR in the range 0.3 – 4 MPa.s^{-1} shall not be designated as « heterogeneous ». They should rather be described as « doubly homogeneous ». Indeed, the dynamics of the vessel pressure and temperature evolution during the depressurization step produces two N-G processes that develop in two successive stages, independently of one another. In each N-G process, the block copolymer (BCP) does homogenize the foam structure.

In Figure 11, the inter-wall nuclei density, noted $N_0^{Inter-wall}$ (see the legend of Figure 11), is plotted as a function of the average PDR (APDR) using a bi logarithmic scale. $N_0^{Inter-wall}$ increases as the APDR is incremented with a threshold effect at 4 Mpa.s^{-1}. The threshold effect is less marked in the foams from 90/10 PMMA/MAM blend saturated at 40°C. The rise of $N_0^{Inter-wall}$as the APDR is increased is much smoother in the foams from PMMA/MAM than in the foams from neat PMMA. This demonstrates again the homogenizing role of an organic BCP such as MAM, which triggers high inter-wall nuclei densities even at low APDR. Using PS or PS/talc systems, Tammaro et al. [24] made similar log-log plots in which the nuclei density linearly increases with APDR. The smoothing effect observed with MAM organic additive is less pronounced with talc inorganic additive. This may be related to the fact that in Tammaro et al. [24], the PS or PS/talc systems are in molten (flowing) state, while our PMMA and PMMA/MAM systems are in a true (non-flowing) solid state.

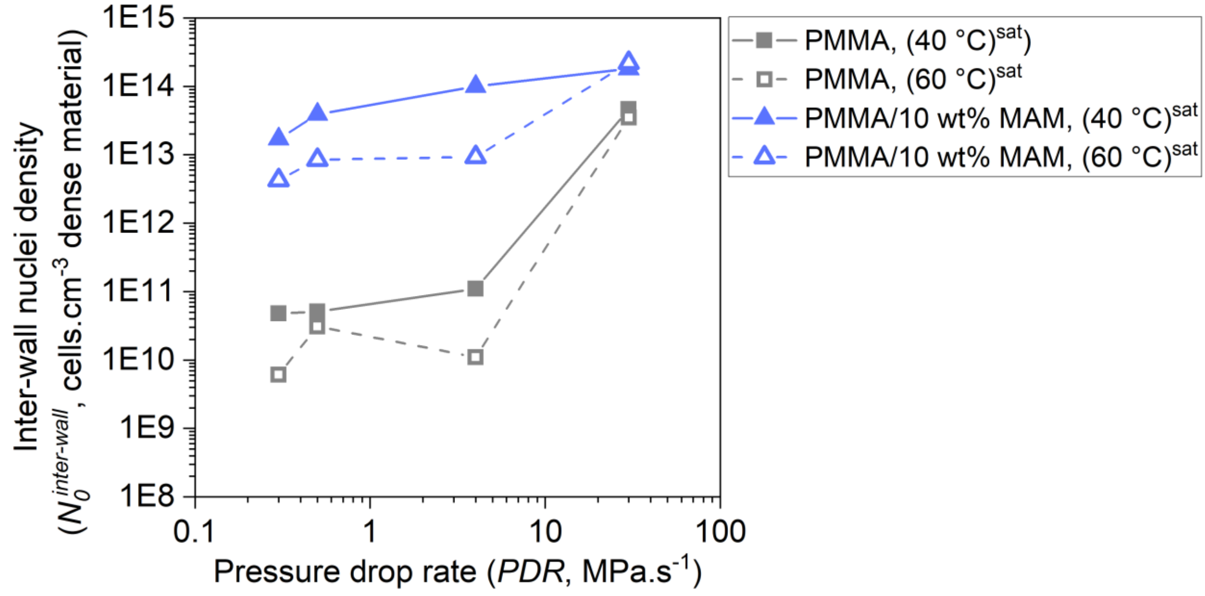

Figure 11. *Inter-wall nuclei density (noted $N_0^{Inter-wall}$) as a function of average PDR (APDR) over 2 decades ranging from 0.3 MPa.s^{-1} to 30 MPa.s^{-1}) in a bi logarithmic scale. In monomodal samples, the inter-wall nuclei density is the usual nuclei density referred to as N_0 in Table 3 and Table 4. In bimodal foam samples (produced from 90/10 PMMA/MAM blend), $N_0^{Inter-wall}$is equal to N_0 multiplied by the Inter-wall cell fraction (Table 5). Saturation temperature is 40 °C or 60°C.*

As for the inter-wall nuclei density, the inter-wall cell mean diameter ($\overline{D}_{inter-wall\ cell}$) (Figure 12) is discriminated by APDR, saturation temperature and MAM presence.

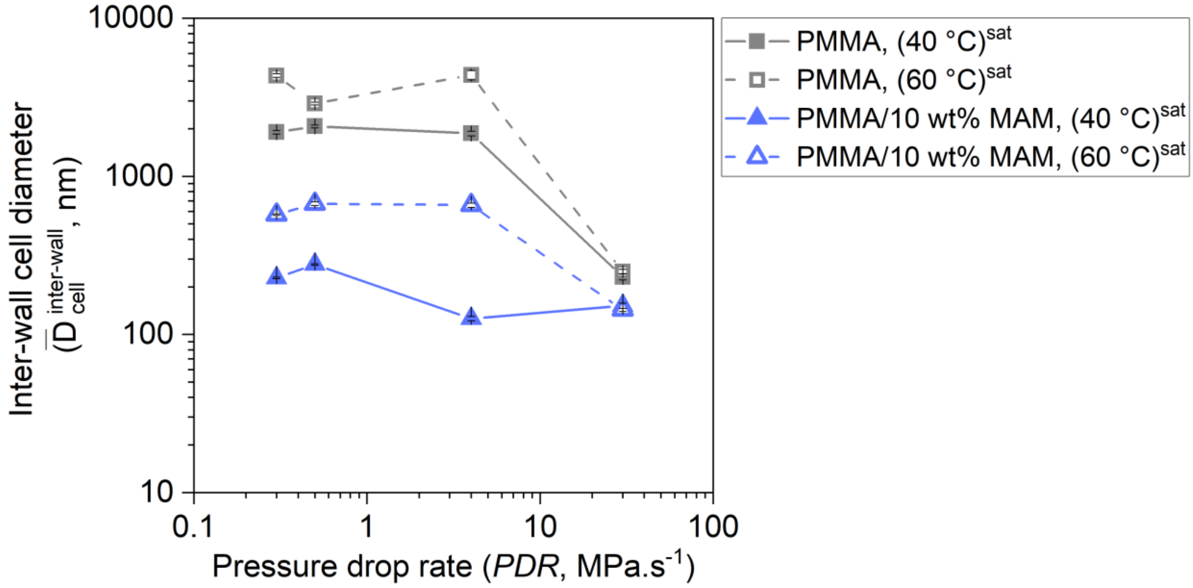

Figure 12. *Mean inter-wall cell size as a function of average PDR (APDR); saturation temperature 40 °C or 60 °C, PMMA and PMMA/10 wt% MAM. In monomodal foam samples, the inter-wall cell mean diameter* $\overline{D}_{inter-wall\ cell}$ *is the average cell diameter* $\overline{D}_{cell}$ *listed in Table 3 and Table 4.*

Over low to intermediate APDR (0.3 to 4 MPa.s^{-1}), MAM enables a gain of 3 decades in ${N_0}^{Inter-wall}$ and a gain of one decade in $\overline{D}_{inter-wall\ cell}$ at fixed saturation temperature (read from the bottom up Figures 11 and 12). Without MAM addition, the APDR is the main factor (the driving force) explaining the reduction by two orders of magnitude of the inter-wall cell diameter (read from left to right Figure 12). With MAM, the APDR appears of secondary importance in the reduction of the porosity dimensions (at a fixed temperature, the inter-wall cell diameter being reduced no more than by a factor two or three; read from left to right Figure 12).

At very high APDR (30 MPa.s^{-1}), the inter-wall nuclei density (Figure 11) and the inter-wall cell diameter (Figure 12) both tend towards similar values without and with MAM addition. This convergence actually expresses different physical phenomena in the case of neat PMMA and in the case of the PMMA/MAM blend. In the former instance, the nuclei density is augmented by a physical phenomenon *i.e.* a steep pressure drop. In the latter case, nucleation is essentially promoted by the concentrating effect of MAM on scCO$_2$.

To our knowledge, the above influence of the APDR upon the final foam structure has been only reported in foaming experiments from the molten state, and not from the solid state as is the case here.

As the APDR is increased, the density (ρ_f) of our acrylic foams also decreases moderately in a comparable manner regardless of the system and the saturation temperature (Figure 13). Although the density remains rather high for foams (> 0.5 g.cm^{-3}), the concomitant decrease of cell diameter (Figure 12) and ρ_f (Figure 13) in a one-step solid-state foaming of *amorphous* acrylics may be viewed as a novelty to the best of our knowledge.

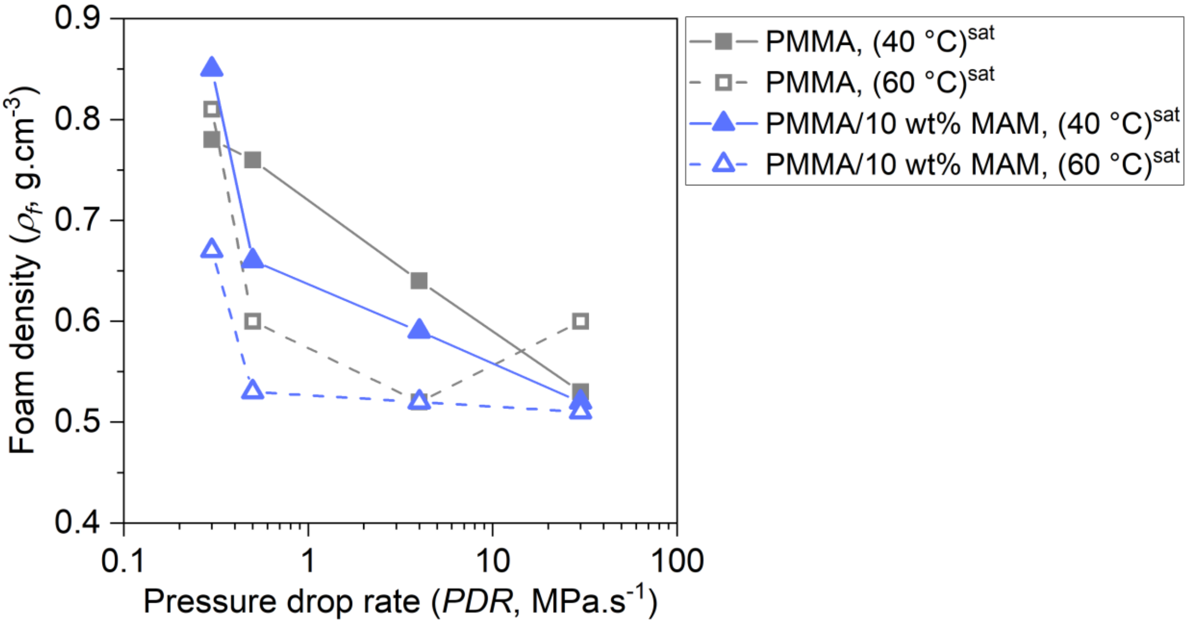

Figure 13. *Evolution of the foam density with the average pressure drop rate (APDR) for neat PMMA and PMMA/10 wt% MAM at two saturation temperatures (40°C and 60 °C).*

Altogether, the trends contained in Figure 11, Figure 12 and Figure 13 can be attributed to the interplay of several kinetics or kinetic factors whose respective effects cannot be unraveled: evolution with time of T^{ef} and that of T_g^{ef}. More precisely, in a one-step procedure, foaming occurs inside the autoclave and the sample effective temperature (T^{ef}) is not controlled right after foaming is triggered. Indeed, depressurization induces a rapid decrease of the sample temperature (T^{ef}), the kinetics of which is not controlled [6],[42],[43] (Figure 10). However, at a certain time of cells development, the actual temperature (T^{ef}) crosses inevitably the effective glass transition temperature of the system (T_g^{ef}), either up or down. At foaming, T_g^{ef} can be much lower than that of neat PMMA before saturation [44]. When $T^{ef} < T_g^{ef}$, the cells are stabilized, this is the vitrification kinetics. Other kinetics may be interfering: phase separation and growth kinetics, kinetics of gas diffusion (either through the bulk matrix phase, but also through interfaces, once MAM nodules are created).

Among the above described numerous triggers for one-step foaming, a « low » CO_2 saturation temperature complying with the supercritical state ($T^{sat} = 40\ °C$ or $60°C$), a PMMA/MAM combination material formulation and a high APDR should be obviously preferred.

3.3 Implications for high thermal insulation

Microsized and nanosized porous polymer foams, in particular those produced using $scCO_2$ as physical foaming agent, are promising thermal insulation *green* materials [1],[2],[45],[46],[44],[47],[48] and ~~for~~ a large variety of applications, including clothing and footwear industries.

The conventional route towards improving thermal insulation of polymer foams (porous materials made of cells/walls/struts) generally consists in *i)* reducing cell size to the nanometer range in order to benefit from the Knudsen effect and *ii)* increasing the expansion ratio (or porosity) since air conductivity is far lower than that of the polymeric lattice [46], [47],[2],[49],[50],[51],[48],[52],[53]. This strategy aims at minimizing the conductive component of the foam effective conductivity k_{ef}. Yet, decreasing cell size and increasing the expansion ratio requires a high number density of cells leading to very thin struts and cell walls which, unfortunately, increase ultimately the radiative transmittivity [54],[55],[48],[52]. Such an increase in the radiative component of the foam effective conductivity k_{ef} often *erases* the performance gain (reduction of the conductive component of k_{ef}) permitted by the Knudsen effect and a high gas fraction [48],[52].

Therefore, the lowered gas conductivity achieved thanks to the Knudsen effect successfully reduces the effective conductivity k_{ef} only in foams showing a relatively high density (e.g ~ 0.3-0.5 g/cm^3) *i.e.* a rather low expansion ratio [52]. The monomodal foams produced in this work from PMMA/10 wt% MAM precursor at high APDR (30 MPa.s^{-1}) after $scCO_2$ saturation at 40°C or 60°C and at moderate APDR (4 MPa.s^{-1}) after saturation at 40°C (Figure 6) exhibit nanosized alveolar cells ($\overline{D}_{cell} <$ 150 nm) and a somewhat high density (~ 0.5 g.cm^{-3}) (table 4). According to the literature cited above and particularly in the line with Buahom et al. [48] and Pang et al. [52], these foams shall show a low effective thermal conductivity.

Using a comprehensive predictive model validated by published experimental data in the literature, Buahom et al. conclude that in low density monomodal foams, the optimal cell-size minimizing the radiative transmittivity (so that the lowered gas conductivity remains meaningful) lies in the micrometer range.

In our view, the bimodal foams produced in our work at low to moderate APDR (0.3 MPa.s^{-1} to 4 MPa.s^{-1}) after $scCO_2$ saturation at 40°C and/or 60°C (Figure 6 and table 5) shall represent a potential innovative solution towards reducing drastically heat transfer. These bimodal samples show locally a porous solid skeleton made up of thick walls and struts and including numerous well apart intra-skeleton nanopores (of a size comparable to that of the micellar nanostructures in the precursor). This locally thick skeleton encapsulates local domains of relatively high-expansion ratio. These local domains are formed either by several adjacent submicrometer-sized cells or reduce to a single submicrometer-sized cell (referred above as inter-wall pores). Within these local domains typified by a high porosity, a submicrometer cell size at which the Knudsen effect starts to take place, the (local) conductive thermal conduction shall be low. At the immediate periphery of these local domains, the larger amount of matter and the well apart nanopores within the thick skeleton shall lower transmittivity (radiative conduction) and the conductive solid conduction[1], respectively. Heat transfer shall be further minimized by the higher tortuosity of the thick skeleton bordering local domains of higher expansion ratio [56],[57],[48]. In addition, the nanosized cells within the thick nanoporous skeleton shall enhance phonon scattering, which increases the solid thermal resistance thereby reducing the solid conductivity [58],[59],[60],[61].

Thus, in this series of bimodal acrylic foams, the benefit from the Knudsen effect within well expanded local domains showing porosity dimensions in the submicrometer range remains meaningful thanks to a locally poorly expanded nanoporous thick solid skeleton *encapsulating* these local domains and preventing radiative thermal conduction from overriding the conductive component at the sample scale.

This suggests that micro-nano bimodal foams may represent better candidates for improved thermal insulation than « all nanosized » foams.

The next step will be to measure the effective conductivity of these thermal insulator polymeric foams. Yet, as recently stressed by Sánchez-Calderón et al. [62], the accurate measurement of the thermal conductivity of micro-nanocellular polymers is quite a challenge which is beyond the scope of the current contribution.

4. Conclusion

With the target of achieving micro-nano foams, this study principally addresses the combined beneficial effects of block copolymer (BCP) addition and high average pressure drop rate (APDR) in one-step solid-state batch $scCO_2$ foaming. Producing micro-nano foams is a multi-factorial issue, where numerous subtle parameters interplay and compete; one can quote the saturation conditions *i.e.* P^{sat} and T^{sat}, the material effective temperature during foaming $T^{ef}(t)$, the effective glass transition temperature of the plasticized system $T_g^{ef}(t)$, the APDR value, and the presence of block copolymer.

APDR and BCP are two key triggering factors. Either parameter may become prevalent for ruling the cell size and the overall density. Over the scrutinized range of saturation temperature (40 °C and 60

---

[1] Heat conduction in the solid is reduced by the significant Knudsen effect in well apart nanopores.

°C), the APDR is the main factor for significantly reducing cell size and increasing nuclei density in foams from neat PMMA. In the block copolymer approach, increasing the APDR appears of secondary importance as the targeted reduction of the porosity dimensions and augmentation of the nuclei density are essentially the consequence of the MAM presence. Yet, in this latter case, increasing the APDR still promotes the « efficiency » of BCP nucleants. In particular, a real efficient nucleation activity of MAM additive is observed at very high average APDR (30 MPa.s^{-1}), leading to unimodal homogeneous distribution of tiny pores, typically 150 nm in diameter, in nearly nanosized foams.

Next, in our saturation conditions ('low' temperature complying with the supercritical sate for CO_2), a high APDR tends to reduce also foam density (although in a moderate way, 0.8 down to 0.5 g.cm^{-3}).

Let us insist again on the fact that in the block copolymer approach, the average PDR (APDR) plays only 'a supporting role' in the final structure of the foam. More precisely, a APDR increment promotes the efficiency of the BCP nucleants. This interplay between BCP and APDR, combined with the underlying instantaneous dynamics dP/dt of the apparent average APDR $\Delta P/\Delta t$, which can be paralleled to a two-stage pressure reduction, can be used to produce bimodal foams where a truly intra-wall/intra-strut nanosized porosity is distinguished from the inter-wall micro-sized pores. Indeed, the evolution with time of the uncontrolled instantaneous depressurization rate dP/dt (Figure 10) leads to two serial nucleation-growth (N-G) processes. Such two N-G processes develop independently of one another. As the (apparent) average PDR($\Delta P/\Delta t$) is higher (as nucleation occurs over a shorter time interval), the earliest N-G process is all the more important to the detriment of the second N-G process, which ends by running out at very high APDR 30 (MPa.s^{-1}). Last we provide some arguments in favor of the superiority of these twofold porosity foams (rather than 'all nano foams') in applications requiring thermal insulation. Indeed, in these double porosity foams, benefit from the Knudsen effect, achieved within well expanded local domains showing submicrometer pores, would remain meaningful thanks to a locally poorly expanded nanoporous thick solid skeleton encapsulating these local domains. Such local encapsulation prevents radiative thermal conduction from overriding the conductive component at the sample scale.

ACKNOWLEDGMENTS This work was supported by the Agence Nationale de la Recherche (ANR, France); grant number AAPG PRCE 2018CE06 0030, 2019; ANR is gratefully acknowledged.

5. References

1. Li, T.; Zhao, G.; Wang, G.; Zhang, L.; Hou, J. Thermal-insulation, Electrical, and Mechanical Properties of Highly-expanded PMMA/MWCNT Nanocomposite Foams Fabricated by Supercritical CO_2 Foaming. *Macromol. Mater. Eng.* **2019**, *304*, 1800789, doi:10.1002/mame.201800789.
2. Notario, B.; Pinto, J.; Solorzano, E.; de Saja, J.A.; Dumon, M.; Rodríguez-Pérez, M.A. Experimental Validation of the Knudsen Effect in Nanocellular Polymeric Foams. *Polymer* **2015**, *56*, 57–67, doi:10.1016/j.polymer.2014.10.006.
3. Coste, G.; Negrell, C.; Caillol, S. From Gas Release to Foam Synthesis, the Second Breath of Blowing Agents. *European Polymer Journal* **2020**, *140*, 110029, doi:10.1016/j.eurpolymj.2020.110029.

4. Park, C.B.; Behravesh, A.H.; Venter, R.D. Low Density Microcellular Foam Processing in Extrusion Using CO2. *Polymer Engineering & Science* **1998**, *38*, 1812–1823, doi:10.1002/pen.10351.
5. Magjarevic, R.; Wu, H.; Krampe, E.; Schlicht, H.; Wintermantel, E. Application of a Microcellular Injection Molding Process (MuCell®) to Produce an Implant with Porous Structure.; Dössel, O., Schlegel, W.C., Eds.; IFMBE Proceedings: Munich, Germany, **2009**; Vol. 25, pp. 61–64.
6. Dumon, M.; Ruiz, J.A.R.; Sanz, J.P.; Perez, M.A.R.; Tallon, J.-M.; Pedros, M.; Cloutet, E.; Viot, P. Block Copolymer-Assisted Microcellular Supercritical CO_2 Foaming of Polymers and Blends. *Cellular Polymers* **2012**, *31*, 207–222, doi:10.1177/026248931203100402.
7. Nalawade, S.P.; Picchioni, F.; Janssen, L.P.B.M. Supercritical Carbon Dioxide as a Green Solvent for Processing Polymer Melts: Processing Aspects and Applications. *Progress in Polymer Science* **2006**, *31*, 19–43, doi:10.1016/j.progpolymsci.2005.08.002.
8. Haurat, M.; Dumon, M. Amorphous Polymers' Foaming and Blends with Organic Foaming-Aid Structured Additives in Supercritical CO_2 , a Way to Fabricate Porous Polymers from Macro to Nano Porosities in Batch or Continuous Processes. *Molecules* **2020**, *25*, 5320, doi:10.3390/molecules25225320.
9. Haurat, M.; Tassaing, T.; Dumon, M. FTIR in Situ Measurement of Swelling and CO2 Sorption in Acrylic Polymers at High CO2 Pressures. *The Journal of Supercritical Fluids* **2022**, *182*, 105534, doi:10.1016/j.supflu.2022.105534.
10. Spitael, P.; Macosko, C.W.; McClurg, R.B. Block Copolymer Micelles for Nucleation of Microcellular Thermoplastic Foams. *Macromolecules* **2004**, *37*, 6874–6882, doi:10.1021/ma049712q.
11. Pinto, J.; Dumon, M.; Pedros, M.; Reglero, J.; Rodriguez-Perez, M.A. Nanocellular CO_2 Foaming of PMMA Assisted by Block Copolymer Nanostructuration. *Chemical Engineering Journal* **2014**, *243*, 428–435, doi:10.1016/j.cej.2014.01.021.
12. Bernardo, V.; Martin-de Leon, J.; Pinto, J.; Catelani, T.; Athanassiou, A.; Rodriguez-Perez, M.A. Low-Density PMMA/MAM Nanocellular Polymers Using Low MAM Contents: Production and Characterization. *Polymer* **2019**, *163*, 115–124, doi:10.1016/j.polymer.2018.12.057.
13. Bernardo, V.; Martin-de Leon, J.; Rodriguez-Perez, M.A. Highly Anisotropic Nanocellular Polymers Based on Tri-Phasic Blends of PMMA with Two Nucleating Agents. *Materials Letters* **2019**, *255*, 126587, doi:10.1016/j.matlet.2019.126587.
14. Costeux, S.; Foether, D. Continuous Extrusion of Nanocellular Foams. In Proceedings of the Conference proceedings Annual Technical Conference-ANTEC; Orlando, **2015**; pp. 2740–2745.
15. Gómez-Monterde, J.; Hain, J.; Sánchez-Soto, M.; Maspoch, M.Ll. Microcellular Injection Moulding: A Comparison between MuCell Process and the Novel Micro-Foaming Technology IQ Foam. *Journal of Materials Processing Technology* **2019**, *268*, 162–170, doi:10.1016/j.jmatprotec.2019.01.015.
16. León, J.M.; Bernardo, V.; Rodríguez-Pérez, M.Á. Key Production Parameters to Obtain Transparent Nanocellular PMMA. *Macromolecular Materials and Engineering* **2017**, 5, doi:10.1002/mame.201700343.
17. Goel, S.K.; Beckman, E.J. Generation of Microcellular Polymeric Foams Using Supercritical Carbon Dioxide. I: Effect of Pressure and Temperature on Nucleation. *Polymer Engineering and Science* **1994**, *34*, 1137–1147, doi:10.1002/pen.760341407.
18. Ruiz, J.A.R.; Pedros, M.; Tallon, J.-M.; Dumon, M. Micro and Nano Cellular Amorphous Polymers (PMMA, PS) in Supercritical CO_2 Assisted by Nanostructured CO_2-Philic Block Copolymers – One Step Foaming Process. *The Journal of Supercritical Fluids* **2011**, *58*, 168–176, doi:10.1016/j.supflu.2011.04.022.
19. Tammaro, D.; Contaldi, V.; Carbone, M.P.; Di Maio, E.; Iannace, S. A Novel Lab-Scale Batch Foaming Equipment: The Mini-Batch. *Journal of Cellular Plastics* **2016**, *52*, 533–543, doi:10.1177/0021955X15584654.
20. Taki, K. Experimental and Numerical Studies on the Effects of Pressure Release Rate on Number Density of Bubbles and Bubble Growth in a Polymeric Foaming Process. *Chemical Engineering Science* **2008**, *63*, 3643–3653, doi:/10.1016/j.ces.2008.04.037.
21. Khan, I.; Costeux, S.; Adrian, D.; Bunker, S. Numerical Studies of Nucleation and Bubble Growth in Thermoplastic Foams at High Nucleation Rates.; Dow Chemical Co., Midland, MI (United States): Seattle, WA (United States), **2013**.
22. Guo, Q.; Mei, Y.; Chang, S.S.Y.; Wang, J.; Park, C.B. Cell Nucleation and Growth Study of PP Foaming with CO_2 in a Batch-Simulation System. *SAE Technical Paper Series* **2006**, doi:10.4271/2006-01-0507.
23. Tammaro, D.; Iannace, S.; Di Maio, E. Insight into Bubble Nucleation at High-Pressure Drop Rate. *Journal of Cellular Plastics* **2017**, *53*, 551–560, doi:10.1177/0021955X17695094.
24. Tammaro, D.; Astarita, A.; Di Maio, E.; Iannace, S. Polystyrene Foaming at High Pressure Drop Rates. *Industrial & Engineering Chemistry Research* **2016**, *55*, 5696–5701, doi:10.1021/acs.iecr.5b04911.
25. Chen, L.; Sheth, H.; Wang, X. Effects of Shear Stress and Pressure Drop Rate on Microcellular Foaming Process. **2001**, *37*, 12, doi:10.1106/VHC8-33K7-M1C7-0M2H.
26. Guo, Q.; Wang, J.; Park, C.B.; Ohshima, M. A Microcellular Foaming Simulation System with a High Pressure-Drop Rate. *Industrial and Engineering Chemistry Research* **2006**, *45*, 6153–6161, doi:10.1021/ie060105w.
27. Shi, B.S.; Li, B.; Nan, Q.Z.; Qin, X.M. Effect of Processing Parameters on Cell Morphology of Polycarbonate Foam. *Plastics, Rubber and Composites* **2011**, *40*, 457–464, doi:10.1179/1743289811Y.0000000004.
28. Muratani, K.; Shimbo, M.; Miyano, Y. Correlation of Decompression Time and Foaming Temperature on the Cell Density of Foamed Polystyrene. *Cellular Polymers* **2005**, *24*, 15–27, doi:10.1177/026248930502400102.

29. Bernardo, V.; Martin-de Leon, J.; Laguna-Gutierrez, E.; Catelani, T.; Pinto, J.; Athanassiou, A.; Rodriguez-Perez, M.A. Understanding the Role of MAM Molecular Weight in the Production of PMMA/MAM Nanocellular Polymers. *Polymer* **2018**, *153*, 262–270, doi:10.1016/j.polymer.2018.08.022.

30. Witkin, A.P. Scale-Space Filtering.; Karlsruhe, Germany, 1983; pp. 1019–1022.

31. Babaud, J.; Witkin, A.P.; Baudin, M.; Duda, R.O. Uniqueness of the Gaussian Kernel for Scale-Space Filtering. In Proceedings of the IEEE Transactions on Pattern Analysis and Machine Intelligence; **1986**; Vol. PAMI-8, pp. 26–33.

32. Koenderink, J.J. The Structure of Images. *Biological Cybernetics* **1984**, *50*, 363–370, doi:10.1007/BF00336961.

33. Laporterie, F.; Flouzat, G.; Amram, O. The Morphological Pyramid and Its Applications to Remote Sensing: Multiresolution Data Analysis and Features Extraction. *Image Analysis and Stereology* **2002**, *21*, 49–53, doi:10.5566/ias.v21.p49-53.

34. Perona, P.; Malik, J. Scale-Space and Edge Detection Using Anisotropic Diffusion. *IEEE Transactions on Pattern Analysis and Machine Intelligence* **1990**, *12*, 629–639, doi:10.1109/34.56205.

35. Canseco, V.; Anguy, Y.; Roa, J.J.; Palomo, E. Structural and Mechanical Characterization of Graphite Foam/Phase Change Material Composites. *Carbon* **2014**, *74*, 266–281, doi:10.1016/j.carbon.2014.03.031.

36. Martinez, E.; Jové Xde la Torre, F.; Santamaria, E. Unsupervised Morphological Segmentation of Objects in Contact.; Grenoble, France, **1997**.

37. Legland, D.; Kiêu, K.; Devaux, M.-F. Computation of Minkowski Measures on 2D and 3D Binary Images. *Image Analysis and Stereology* **2007**, *26*, 83–92, doi:10.5566/ias.v26.p83-92.

38. Costeux, S. CO_2-Blown Nanocellular Foams. *Journal of Applied Polymer Science* **2014**, *131*, 1–16, doi:10.1002/app.41293.

39. Kaneko, K. Determination of Pore Size and Pore Size Distribution 1. Adsorbents and Catalysts. *Journal of Membrane Science* **1994**, *96*, 59–89, doi:/10.1016/0376-7388(94)00126-X.

40. Pinto, J.; Reglero-Ruiz, J.A.; Dumon, M.; Rodriguez-Perez, M.A. Temperature Influence and CO_2 Transport in Foaming Processes of Poly(Methyl Methacrylate)–Block Copolymer Nanocellular and Microcellular Foams. *The Journal of Supercritical Fluids* **2014**, *94*, 198–205, doi:10.1016/j.supflu.2014.07.021.

41. Arora, K.A.; Lesser, A.J.; McCarthy, T.J. Preparation and Characterization of Microcellular Polystyrene Foams Processed in Supercritical Carbon Dioxide. *Macromolecules* **1998**, *31*, 4614–4620, doi:10.1021/ma971811z.

42. Reglero Ruiz, J.A.; Dumon, M.; Pinto, J.; Rodriguez-Pérez, M.A. Low-Density Nanocellular Foams Produced by High-Pressure Carbon Dioxide. *Macromolecular Materials and Engineering* **2011**, *296*, 752–759, doi:10.1002/mame.201000346.

43. Reglero Ruiz, J.A.; Saiz-Arroyo, C.; Dumon, M.; Rodríguez-Perez, M.A.; Gonzalez, L. Production, Cellular Structure and Thermal Conductivity of Microcellular (Methyl Methacrylate)-(Butyl Acrylate)-(Methyl Methacrylate) Triblock Copolymers: Microcellular MAM Triblock Copolymers. *Polymer International* **2011**, *60*, 146–152, doi:10.1002/pi.2931.

44. Ruiz, J.A.R.; Viot, P.; Dumon, M. Foaming Behaviour and Compressive Properties of Microcellular Nanostructured Polystyrene. *Cellular Polymers* **2009**, *28*, 363–385, doi:10.1177/026248930902800601.

45. Forest C., Chaumont P., Cassagnau P., Swoboda B., Sonntag P., CO_2 nano-foaming of nanostructured PMMA. *Polymer* **2015**, *58,* 76–87, doi.org/10.1016/j.polymer.2014.12.048.

46. Forest, C., Chaumont, P., Cassagnau, P., Swoboda, B., Sonntag P., Polymer nano-foams for insulating applications prepared from CO_2 foaming, *Prog. Polym. Sci.* **2015**, *41*, 122–145, doi.org/10.1016/j.progpolymsci.2014.07.001.

47. Notario, B., Pinto, J., Rodriguez-Perez, M. A., Nanoporous polymeric materials: A new class of materials with enhanced properties. *Prog. Mater. Sci.* **2016**, *78–79*, 93–139, doi.org/10.1016/j.pmatsci.2016.02.002.

48. Buahom, P., Wang, C., Alshrah, M., Wang, G., Gong, P., Tran M.-P., Park, C. B., Wrong expectation of superinsulation behavior from largely-expanded nanocellular foams. *Nanoscale*, **2020**, *12*, 13064–13085, doi.org/10.1039/d0nr01927e.

49. Rizvi, A., Chu, R. K. M., Park, C.B., Scalable fabrication of thermally insulating mechanically resilient hierarchically porous polymer foams. *ACS Appl. Mater. Interfaces* **2018**, *10*(44), 38410–38417, doi.org/10.1021/acsami.8b11375.

50. Wang, G., Zhao, J., Wang, G., Mark, L. H., Park, C. B., Zhao, G., Low-density and structure-tunable microcellular PMMA foams with improved thermal-insulation and compressive mechanical properties. *Eur. Polym. J.* **2017,** *95,* 382–393, https://doi.org/10.1016/j.eurpolymj.2017.08.025.

51. Wang, L., He, Y., Jiang T., Zhang, X., Zhang, C., Peng, X., Morphologies and properties of epoxy/multi-walled carbon nanotube nanocomposite foams prepared through the free-foaming and limited-foaming process. *Compos. Sci. Technol.* **2019**, *182*, 107776, https://doi.org/10.1016/j.compscitech.2019.107776

52. Pang, Y., Cao, Y., Zheng, W., Park C. B., A comprehensive review of cell structure variation and general rules for polymer microcellular foam. *Chemical Engineering Journal* **2022**, *430,* 132662, https://doi.org/10.1016/j.cej.2021.132662.

53. Shi, Z., Zhao, G., Lei Zhang, L. Wang, G., Chai J., Ultralight and hydrophobic PVDF/PMMA open-cell foams with outstanding heat-insulation and oil-adsorption performances fabricated by CO_2 molten foaming. *Journal of CO2 Utilization* **2022***, 63*, 102108, https://doi.org/10.1016/j.jcou.2022.102108.

54. Wang, G., Wang, C., Zhao, J., Wang, G., Park, C. B., Zhao G., Modelling of thermal transport through a nanocellular polymer foam: toward the generation of a new superinsulating material. *Nanoscale* **2017,** *9*, 5996–6009. doihttps://doi.org/10.1039/C7NR00327G

55. Wang, G., Wang, C., Zhao, J., Wang, G., Park C. B., Zhao G., Van De Walle W., Janssen H, Correction: Modelling of thermal transport through a nanocellular polymer foam: Toward the generation of a new superinsulating material. *Nanoscale* **2018***, 10,* 20469–20473, doi.org/10.1039/C8NR90192A

56. Glicksman, L. R., Torpey, M. Factors governing heat transfer through closed cell foam insulation. *J. Therm. Insul.* **1989**, *12*, 257–269, doi.org/10.1177/109719638901200

57. Glicksman, L. R., Torpey, M., Marge, A. Means to improve the thermal conductivity of foam insulation. *J. Cell. Plast.* **1992**, *28,* 571–583, doi.org/10.1177/0021955X9202800

58. Zhao, J., Zhao Q., Wang, L., Wang C., Guo B., Park, C. B., Wang, G,. Development of high heat insulation and compressive strength BPP foams using mold-opening foam injection molding with in-situ fibrillated PTFE fibers. *Eur. Polym. J.* **2018***, 98*, 1–10, https://doi.org/10.1016/j.eurpolymj.2017.11.001.

59. Hou, J., Zhao, G., Wang, G., Zhang, L., Dong, G., Li, B., Ultra-high expansion linear polypropylene foams prepared in a semi-molten state under supercritical CO_2, *J. Supercrit. Fluids* **2019***, 145,* 140–150, https://doi.org/10.1016/j.

60. Yin, D., Mi, J., Zhou, H., Wang, X., Tian, H. Fabrication of branching poly (butylene succinate)/cellulose nanocrystal foams with exceptional heat insulation, *Carbohydr. Polym.* **2020**, *247*,116708–116717, https://doi.org/10.1016/j.

61. Shi, Z., Zhao, G., Lei Zhang, L., Wang, G., Chai, J., Ultralight and hydrophobic PVDF/PMMA open-cell foams with outstanding heat-insulation and oil-adsorption performances fabricated by CO_2 molten foaming. *Journal of CO2 Utilization* **2022**, *63*, 102108, doi.org/10.1016/j.jcou.2022.102108.

62. Sánchez-Calderón, I., Sillero, Á., Lizalde-Arroyo, F., Bernardo, V., Martín-de-León, J., Rodríguez-Pérez, M. J. **2023**. Evaluation of methods to accurately characterize the thermal conductivity of micro-and nanocellular polymers based on poly(methyl-methacrylate) (PMMA) produced at lab-scale. *Polymer Testing* **2023***, 117,* 107842, https://doi.org/10.1016/j.polymertesting.2022.107842.